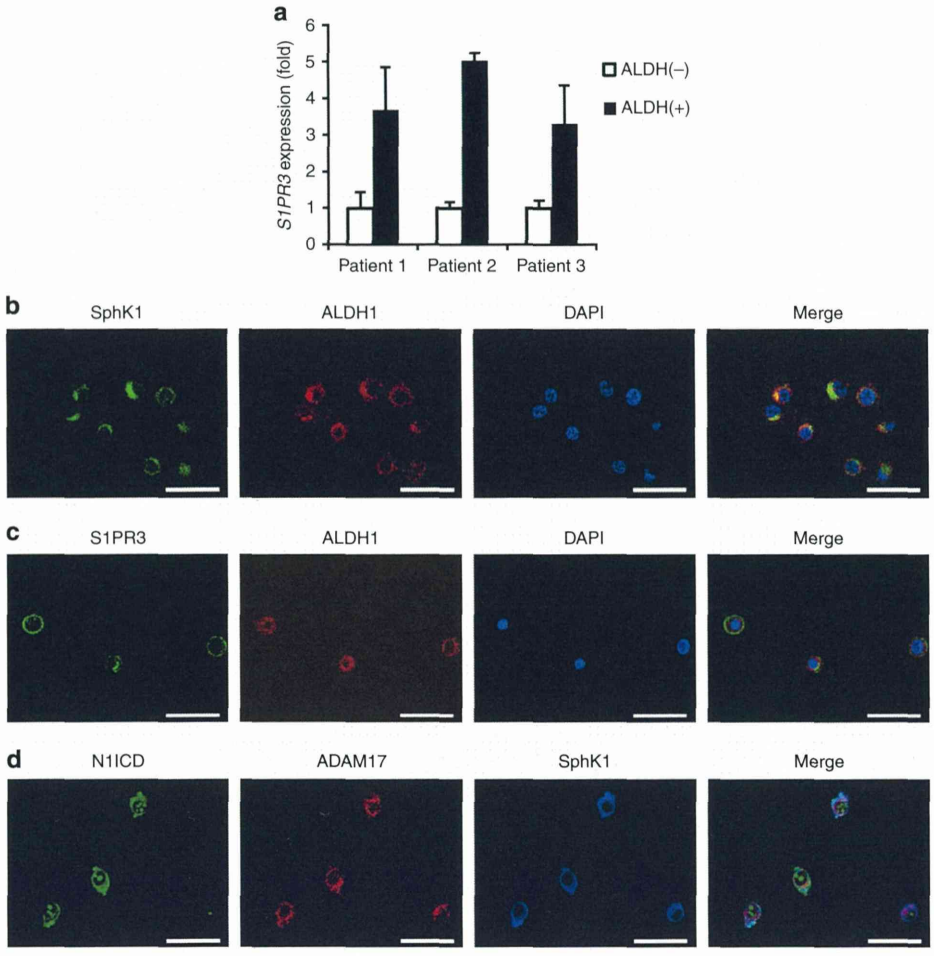

Figure 7 | SphK1-positive CSCs in human breast cancers. (**a**) *S1PR3* expression in the ALDH-negative or ALDH-positive patient-derived cells by qPCR. Expression levels were normalized to glyceraldehyde 3-phosphate dehydrogenase messenger RNAs. Data represent mean ± s.d. ($n = 3$). (**b**) Double immunostaining of SphK1 (green) and ALDH1 (red) in patient-derived tumour cells. Nuclei were counterstained by DAPI (blue). (**c**) Double immunostaining of S1PR3 (green) and ALDH1 (red) in patient-derived tumour cells. Nuclei were counterstained by DAPI (blue). (**d**) Triple immunostaining of N1ICD (green), ADAM17 (red) and SphK1 (blue) in patient-derived tumour cells. Scale bar, 20 μm.

between the S1PR and ADAM17 activation in Notch ligands-independent manner. Further studies should be conducted looking at how the Notch system induces CSC phenotypes in breast cancer.

Our data demonstrate an essential cell autonomous role of Notch1 in breast CSCs expansion. Harrison *et al.*[42] has reported that Notch4 also affects breast CSCs. They performed knockdown of Notch paralog (Notch1 and Notch4) using both $ESA^+/CD44^+/CD24^{low}$ and mammosphere prepared from MCF-7 cells, although Notch ICD overexpression was not examined. Notch1 knockdown reduced only mammosphere population, whereas Notch4 knockdown reduced both $ESA^+/CD44^+/CD24^{low}$ and mammosphere populations (as shown in Figs 3a and 4b). Because Ginestier *et al.*[4] have already reported that two stem-like cell populations defined by ALDH positive and $CD44^+/CD24^-/lin^-$ were not identical, there is a possibility that discrepancy between our present data and Harrison's report is caused by the differences of cell populations used in the experiments. Thus, Notch paralog possibly plays a role in regulation in different stem cell population.

Our clinical samples suggest the crosstalk between Sphk1-S1P-S1PR3 and Notch signalling by co-localization of the components for the crosstalk machinery. Similar observations were obtained using xenografted tumour samples in nude mice. SphK1 has been already shown to be upregulated in patients with breast cancer[43], and its expression correlates with cancer progression and poor prognosis[43–45]. In addition, S1PR3 is the most highly expressed S1PR in breast cancer cells[46]. Thus, our data provide a potential explanation for significance of Sphk1-S1PR3-Notch axis in breast cancer.

Targeting Notch has been expected to facilitate tumour regression[47]. Although several types of Notch inhibitors are quite effective in preclinical models[21,48,49], none of the clinical trials conducted so far has examined effectiveness[50]. This prompts us to encourage efforts to explore alternative/additional approaches for targeting Notch. Our evidence suggests that Notch1 is involved in the S1P-induced CSC phenotype. Because lipid signalling acts upstream of the Notch, S1PR3 could be a promising target for various cancer. Indeed, TY52156 inhibited the tumorigenicity of SphK1-overexpressing breast CSCs (Fig. 6). Although several S1PR antagonists are currently available[14], few have been tested in clinical trials. The feasibility of S1PR3 antagonists in cancer remains to be determined.

In conclusion, the identification of S1P-derived CSC phenotype is required for continuous tumour growth, and points to potential

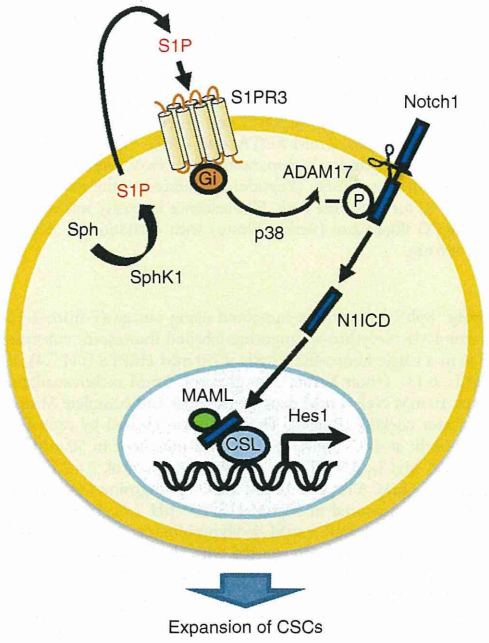

Figure 8 | A working model for the functions of SphK/S1P/S1PR3 in CSC regulation. S1P produced by SphK1 stimulates S1PR3 and subsequently activates Notch signaling in a Notch ligand-independent manner. Activation of S1P signaling pathway leads to expansion of CSCs.

culprits of tumour formation in patients. In the future, it might be possible to establish specific treatments that reduce tumorigenesis by targeting 'stemness' in cancer. Thus, efforts should be made to develop drugs capable of inhibiting CSC self-renewal and expansion by S1PR3.

Methods

Materials. Antibodies to p38MAPK (#9212), phospho-p38MAPK (#9211), Akt (#9272), phospho-Akt (#9271), Notch1 (#4380), N1ICD (#2421) and Notch3 (#2889) were from Cell Signaling Technology. Antibodies to HA (#H6908), FLAG (M2) (#F1804), myc (#C3956), β-actin (#A5441) and ADAM17 (phospho-Thr735) (#SAB4504073) were from Sigma-Aldrich. Antibody to ADAM17 (#AB19027) was from Millipore. Antibody to APC-conjugated TRA-1-85 (#FAB3195A) was from R&D Systems. Antibody to SphK1 (#AP7237c) was from Abgent. Antibody to ALDH1 (#611194), FITC mouse anti-human CD44 (#555478), PE mouse anti-human CD24 (#555428), FITC mouse IgG2b κ isotype control (#555742) and PE mouse IgG2a κ isotype control (#555574) were from BD Biosciences. Antibodies to S1PR2 (#sc-25491), S1PR3 (#sc-30024) and Spns2 (#130102) were from Santa Cruz Biotechnology. Antibody to SphK1 (#ab46719), ADAM17 (#ab57484), activated Notch1 (#ab8925) and ABCC1 (#ab3368) were from Abcam. Antibody to Alexa488-conjugated anti-rabbit IgG (#A11034) and Alexa555-conjugated anti-mouse IgG (#A21424) were from Invitrogen. S1P, dihydro-S1P, DAPT, SB203580, 5-Fluorouracil and doxorubicin were from Enzo Life Sciences. CAY10444, JTE013, MK571, LY294002, cyclopamine were from Cayman Chemicals. LPA was from Avanti Polar Lipids. Jagged1-Fc, Sonic hedgehog and Wnt3a were from R&D Systems. Botulinum C3 enzyme was from Bio Academia. PTX were from Wako Pure Chemical (Osaka, Japan). Hoechst, reserpine, DFO and PNU74654 were from Sigma-Aldrich, while N,N′-bis(4-chlorophenyl)-3,3-dimethyl-2-oxobutanehydrazonamide (TY52156) was synthesized. All other reagents were of analytical grade and obtained from commercial sources.

Cell culture. MCF-7 cells (American Type Culture Collection), MDA-MB-231 cells (American Type Culture Collection), A549 cells (European Collection of Cell Cultures) and LNCaP cells (European Collection of Cell Cultures), U251 cells (Japanese Collection of Research Biosources) were cultured in Dulbecco's modified Eagle's medium (DMEM; Sigma-Aldrich) supplemented with 10% heat-inactivated fetal bovine serum (FBS; Biological Industries), 100 U ml^{-1} penicillin and 100 μg ml^{-1} streptomycin (Gibco BRL). OVCAR-5 cells was cultured in RPMI1640 (Sigma-Aldrich) supplemented with 10% heat-inactivated FBS (Biological Industries), 100 U ml^{-1} penicillin and 100 μg ml^{-1} streptomycin (Gibco BRL).

Plasmid constructs and reporter assays. Plasmids encoding SphK1, SphK2, DN-CSL, DN-MAML, N1ICD, ADAM10 and 12xCSL-luc were kindly provided from Drs Stuart M. Pitson (University of Adelaide), Taro Okada (Kobe University), Aly Karsan (British Columbia Cancer Research Centre), Anthony J. Capobianco (University of Pennsylvania), Spyros Artavanis-Tsakonas (Harvard Medical School), Stefan Lichtenthaler (Ludvig Maximilians University) and Lothar J. Strobl (German Research Center for Environmental Health), respectively. Plasmids encoding N2ICD, N3ICD and N4ICD were kindly provided by Dr Michael J. Hendzel (University of Alberta). Plasmids encoding ADAM17 and DN-ADAM17 were kindly provided by Dr Rik Derynck (University of California, San Francisco). Plasmids encoding CA-G_i and CA-G_{12} were kindly provided by Dr J. Silvio Gutkind (National Institutes of Health). Plasmids encoding the ADAM17 mutants T735A and T761A were generated by QuikChange Site-Directed Mutagenesis (Stratagene) using pRK5-ADAM17-myc. A plasmid encoding the ADAM10 mutant E384A (DN-ADAM10) was generated by QuikChange Site-Directed Mutagenesis using peak-12-ADAM10-HA. Coding DNA sequences were verified by DNA sequencing. Transfections were conducted with FuGENE HD transfection reagent (Promega). Luciferase activity was assayed 24 h after transfection with 12xCSL-luc using the Glo Luciferase Assay Kit (Promega).

Microarray analysis. Total RNAs were isolated by Trizol (Invitrogen) and then purified using an RNeasy Mini Kit (Qiagen). Affymetrix Genome U133A gene chips (Affymetrix) were used to examine gene expression patterns according to the manufacturer's instruction. Genes upregulated more than twofold are shown in Supplementary Data 1.

ALDH assays. The ALDEFLUOR kit (Stem Cell Technologies) was used to detect CSC populations with high ALDH enzyme activity according to the manufacture's instruction[18]. The cells were plated at a density of 3×10^5 cells in 100 mm culture dishes. After serum deprivation for 3 days, cells were suspended at a concentration of 1×10^6 cells ml^{-1} in ALDH assay buffer containing the ALDH substrate BAAA (1 μM) and incubated for 30 min at 37 °C. As a negative control, cells were treated with diethylaminobenzaldehyde (15 μM), a specific ALDH inhibitor. A FACS Aria II cell sorter (BD Biosciences) was used to measure the ALDH-positive cell population.

Mammosphere-forming assays. MCF-7 cells were plated as single cells on ultralow attachment 6-well plates (Corning) at a concentration of 10,000 cells ml^{-1} in serum-free DMEM supplemented with N_2 supplement (Gibco) and 20 ng ml^{-1} basic Fibroblast Growth Factor (R&D Systems). After 4 days, the number of mammospheres was microscopically counted and the percentage of mammosphere-forming cells was determined as mammosphere-forming efficiency (%)[7].

SP assays. Cells were collected and suspended in prewarmed DMEM containing 2% FBS and 2 mM HEPES buffer. Hoechst 33342 dye (Sigma-Aldrich) was then added to a final concentration of 5 μg ml^{-1}, and the mixture was incubated with intermittent shaking for 60 min at 37 °C in the presence or absence of reserpine (15 μg ml^{-1}; Sigma-Aldrich). Cells were then resuspended in ice-cold phosphate-buffered saline (PBS) containing 2% FBS, and analysed with a FACS Aria II cell sorter (BD Biosciences).

CD44$^+$/CD24$^-$ cell population. Cells were resuspended in PBS containing 5% FBS and incubated with FITC mouse anti-human CD44 (#555478, 1:5) and PE mouse anti-human CD24 (#555428, 1:5) for 15 min at 4 °C. FITC mouse IgG2b κ isotype control (#555742, 1:5) and PE mouse IgG2a κ isotype control (#555574, 1:5) were used as negative control. Analysis was performed using a FACS Aria II cell sorter (BD Biosciences).

Cell viability assays. MCF-7 cells and sorted ALDH-positive cells were plated onto 96-well plates at a density of 5,000 cells well^{-1}. After overnight culture, cells were treated with 100 μM 5-Fluorouracil or 10 μM doxorubicin. After 72 h, MTS assays were performed, according to the manufacturer's instruction (Promega).

qPCR assays. Total RNA was isolated from MCF-7 cells using Trizol (Invitrogen), according to the manufacturer's instructions. The qPCR assays were conducted with the aid of a QuantiTect SYBR Green RT-PCR Kit (Qiagen) and an ABI PRISM 7900HT sequence detection system (Applied Biosystems). The relative changes in transcript levels for each sample were determined by normalizing to glyceraldehyde 3-phosphate dehydrogenase mRNA levels. Primer sequences used for qPCR analysis are shown in Supplementary Table 2.

Reverse transcription PCR analysis of S1PRs. Total RNA was isolated from MCF-7 cells using Trizol, according to the manufacturer's instructions. A SuperScript III Fast-Strand Synthesis System (Invitrogen) was used for reverse transcription synthesis of cDNAs. PCR amplification was performed with PrimeStar HS DNA polymerase (Takara) using GeneAmp PCR System 9700 (Applied

Biosystems). The cycling conditions were as follows: 1 min at 95 °C, 40 cycles of 30 s at 95 °C, 30 s at 54–66 °C, 1 min at 72 °C, following 7 min at 72 °C. Primer sequences used for reverse transcription PCR analysis are shown in Supplementary Table 2.

Transient RNA interference. Double-strand RNA oligonucleotides (siRNAs) against *S1PR3*, *S1PR2* and appropriate control scrambled siRNA were from Santa Cruz Biotechnology. The siRNAs against *Notch1*, *ABCC1* and *Spns2* were from Invitrogen. The siRNAs were transfected into MCF-7 cells using RNAiMax (Invitrogen) according to the manufacturer's recommendations.

Stable knockdown by lentiviral shRNA transduction. For stable gene silencing of *S1PR3* or *S1PR2*, specific shRNA MISSION lentiviruses (Sigma-Aldrich) were transduced into cells. The target sequence was 5′-CCGGGATCCTCTACGCAC GCATCTACTCGAGTAGATGCGTGCGTAGAGGATCTTTTTG-3′ for sh*S1PR3* and 5′-CCGGACTTTACCACCTGGTACAAAGCTCGAGCTTTGTACCAGGTG GTAAAGTTTTTTG-3′ for sh*S1PR2*. The transduced cells were selected in growth medium containing 1.5 μg ml^{-1} puromycin (Sigma-Aldrich).

Immunoblot analysis. Cells were lysed in Cell Lysis Buffer (Cell Signaling Technology) on ice for 30 min. Lysates were subjected to sodium dodecyl sulphate polyacrylamide gel electrophoresis and transferred to Immobilon-P Transfer Membrane (Millipore). Membranes were blocked with 5% (w/v) bovine serum albumin in Tris-buffered saline containing 0.1% Tween-20 (TBST) and incubated with primary antibodies overnight at 4 °C. Membranes were then incubated with horseradish peroxidase-conjugated secondary antibodies (Cell Signaling Technology, 1:2,000) for 1 h at room temperature and detected using ECL Prime Western Blotting Detection Reagent (GE Healthcare). Images were acquired using a LAS-3000 Imager (Fujifilm). The density of each band was quantified using an image analyser (Multi Gauge software, Fujifilm). The primary antibodies used were S1PR3 (#sc-30024, 1:2,000), S1PR2 (#sc-25491, 1:1,000), Notch1 (#4380, 1:1,000), N1ICD (#2421, 1:1,000), Notch3 (#2889, 1:1,000), FLAG (#F1804, 1:1,000), myc (#C3956, 1:5,000), HA (#H6908, 1:1,000), phospho-ADAM17 (#SAB4504073, 1:1,000), ADAM17 (#AB19027, 1:1,000), phospho-p38MAPK (#9211, 1:1,000), p38MAPK (#9212, 1:1,000), phospho-Akt (#9271, 1:1,000), Akt (#9272, 1:1,000), SphK1 (#AP7237c, 1:500), SphK2 (a gift from Dr T. Okada at Kobe University, 1:3,000), ABCC1 (#ab3368, 1:1,000), Spns2 (#sc-130102, 1:1,000) and β-actin (#A5441, 1:10,000). Original immunoblots are shown in Supplementary Fig. 19.

Immunocytochemistry. SphK-overexpressing MCF-7 cells and mammosphere cells were plated on glass coverslips. Cells were fixed with 4% paraformaldehyde and permeabilized with 0.2% Triton X-100. Coverslips were blocked with 5% FBS and incubated overnight at 4 °C with primary antibodies that recognized FLAG (#F1804, 1:500), HA (#H6908, 1:120), SphK1 (#ab46719, 1:50), S1PR3 (#sc-30024, 1:50), ALDH1 (#611194, 1:100). ADAM17 (#ab57484, 1:300) and activated Notch1 (#ab8925, 1:200). After rinsing with PBS, coverslips were incubated for 1 h at room temperature with Alexa488-conjugated (#A11034, 1:200) or Alexa555-conjugated (#A21424, 1:200) secondary antibody. In the case of triple staining of Sphk1, ALDH1 and N1ICD, antibody to SphK1 was labelled with AMCA conjugation kit (Abcam). After rinsing with PBS, coverslips were incubated with AMCA-conjugated SphK1 antibody (1:100) for 1.5 h. Nuclei were counterstained with DAPI (Nacalai Tesque). Fluorescence images were obtained using a Nikon A1 confocal microscope (Nikon).

Immunoprecipitation assay. Immunoprecipitation was conducted as previously reported with slight modifications[51]. MCF-7 cells were transfected with myc-tagged ADAM17. At 48 h after transfection, cells were lysed in lysis buffer (20 mM Tris–HCl pH 7.4, 200 mM NaCl, 0.1% NP-40, 10 mM NaF, 1 mM Na_3VO_4 and complete mini protease inhibitor cocktail (Roche Applied Sciences)). Lysates (100 μg) were incubated with myc-specific polyclonal antibody (#C3956, 1 μg) or normal rabbit IgG (#PM035, MBL, 1 μg) overnight at 4 °C. Subsequently, Protein G Sepharose (Amersham Pharmacia Biotech) was added to the mixture and incubated for an additional 2 h at 4 °C. Beads were washed with lysis buffer and immunoprecipitated proteins analysed by immunoblotting using a p38MAPK-specific polyclonal antibody (#9212) and a myc-specific polyclonal antibody (#C3956).

ADAM17 activity. ADAM17 activity was measured using a SensoLyte 520 ADAM17 Activity Assay Kit (ANASPEC) according to the manufacture's instruction[52]. MCF-7 cells were scraped in PBS containing a complete mini protease inhibitor cocktail and lysed using five cycles of freeze–thawing. Lysed cells were centrifuged at 20,000 *g* for 15 min and pelleted membranes resuspended with assay buffer. Approximately 15 μg of proteins were mixed with substrate for 30 min and fluorescence intensity was measured using a Wallac1420ARVO fluoroscan (Perkin Elmer), with excitation at 490 nm and emission at 520 nm.

γ-secretase activity. The activity of γ-secretase was measured using a specific fluorogenic substrate assay[53]. Cells were collected in cell lysis buffer containing (20 mM HEPES pH 7.0, 150 mM KCl, 2 mM EDTA, 1% (3-cholamidopropyl) dimethylammonio]-2-hydroxy-1-propanesulfonate (CHAPSO; Dojindo Laboratories), and complete Mini, EDTA-free protease inhibitor cocktail (Roche)). Lysates were centrifuged at 10,000 *g* for 1 min at 4 °C to remove nuclei and large cell debris. Approximately 5 μg of protein was added to each well of a white 96-well polystyrene microplate (Packard) and an equal volume of assay buffer (50 mM Tris–HCl (pH 6.8), 2 mM EDTA, and 0.25% (3-cholamidopropyl) dimethylammonio]-2-hydroxy-1-propanesulfonate (w/v)) added. 10 μM fluorogenic γ-secretase substrate (Peptide) was added to the plate and samples incubated at 37 °C for 4 h in the dark. Fluorescence intensity was measured using a Wallac1420ARVO fluoroscan (Perkin Elmer) with excitation at 355 nm and emission at 460 nm.

SphK activity. SphK activity was measured using omega-(7-nitro-2-1,3-benzoxadiazol-4-yl)-D-erythro-sphingosine-labelled fluorescent substrate[54]. Cells were lysed with a single freeze–thaw cycle in 50 mM HEPES (pH 7.4), 10 mM KCl, 15 mM $MgCl_2$, 0.1% Triton X-100, 20% glycerol, 2 mM orthovanadate, 2 mM dithiothreitol, 10 mM NaF, 1 mM deoxypyridoxine and complete Mini, EDTA-free protease inhibitor cocktail (Roche). The lysate was cleared by centrifuging at 20,000 *g* for 15 min at 4 °C. SphK1 activity was measured in 50 mM HEPES (pH 7.4), 15 mM $MgCl_2$, 0.5% Tríton X-100, 10% glycerol, 5 mM NaF, 1 mM deoxypyridoxine, 2 mM ATP and 10 μM NBD-sphingosine (Avanti Polar Lipids). SphK2 activity was measured in 50 mM HEPES (pH 7.4), 15 mM $MgCl_2$, 0.5 M KCl, 10% glycerol, 5 mM NaF, 1 mM deoxypyridoxine, 2 mM ATP and 10 μM NBD- sphingosine. Reactions were started with the addition of 5 μg of lysate protein and incubated for 4 h at room temperature. Reactions were extracted with the addition of 1 M potassium phosphate (pH 8.5), followed by chloroform/methanol (2:1), then cleared at 15,000 *g* for 1 min. The upper aqueous layer was placed into the wells of white 96-well polystyrene microplates (Packard). Fluorescence intensity was measured with a Wallac1420ARVO fluoroscan (Perkin Elmer) with excitation at 485 nm and emission at 535 nm.

Tumorigenicity assay. The animal study protocol was reviewed and approved by the animal care and use committee of the institute. Six-week-old female Balb/c nude mice (CLEA Japan) were used in these studies and were given injections of 17-β-estradiol (Sigma-Aldrich) dissolved in pure sesame oil (0.1 mg 0.05 ml^{-1} sesame oil per mouse, subcutaneously) 1 day before tumour inoculation, and at weekly intervals, according to a previously reported protocol with slight modifications[55]. The ALDH-positive cell population was sorted by FACS (BD Aria II) and suspended in PBS mixed with an equal volume of Matrigel (BD Biosciences). Mice were given bilateral subcutaneous injections of 1×10^5 (0.1 ml) cells. Tumour growth was monitored for 6 weeks and analysed. Tumour volume was determined using the formula: $V = ½ \times$ larger diameter $\times$ (smaller diameter)^2.

For the immunohistochemistry, paraffin-embedded sections of breast tumours from xenografts were deparaffinized in xylene and rehydrated in graded alcohol. Antigen retrieval was conducted three times by microwaving the slides in 0.01 M citrate buffer (pH 6.0) for 5 min. Sections were blocked with 5% FBS and incubated for 1.5 h with primary antibodies that recognized S1PR3 (#sc-30024, 1:50) and ALDH1 (#611194, 1:100). After rinsing with PBS, coverslips were incubated for 1 h at room temperature with Alexa488-conjugated (#A11034, 1:200) or Alexa555-conjugated (#A21424, 1:200) secondary antibody. Nuclei were counterstained with DAPI (Nacalai Tesque). Fluorescence images were obtained using a Bioreve BZ-9000 (Keyence). The number of S1PR3- and ALDH1 double-positive cells was counted in five fields[56].

For the hierarchy assay, the xenografts were collected after 6 weeks, dissociated into single cells and TRA-1-85-positive cells analysed using the ALDH assays[57]. Single cells were suspended in ALDH assay buffer containing the BAAA (1 μM) and incubated 30 min at 37 °C. The cells were resuspended in ALDH assay buffer for subsequent staining with the APC-conjugated TRA-1-85 antibody (#FAB3195A, 1:10), which recognizes human cells and thereby allows their discrimination from mouse cells. After incubation for 30 min and following centrifugation, the cells were resuspended in ALDH assay buffer containing 7-AAD (BD Bioscience, #559925) and analysed with a FACS Aria II cell sorter (BD Bioscience).

For the chronic administration, TY52156 (167 mg ml^{-1} in a 1:1 mixture of DMSO and PEG400) was inserted in subcutaneously implanted Alzet osmotic pumps (Cupertino), designed to release TY52156 continuously (at about 25 μg h^{-1}) for 6 weeks.

Mammosphere formation from primary cells. Mammosphere formation using primary cells (Celprogen) was performed[7,8]. The cells were plated as single cells in ultralow attachment dishes (Corning) at a density of 20,000 viable cells ml^{-1} in mammary epithelial growth medium for 7 days. To make secondary mammospheres, primary mammospheres were collected by gentle centrifugation (200*g*), dissociated enzymatically (10 min in 0.05% trypsin–EDTA) and mechanically (pipetting with yellow tips) into a single-cell suspension. The cells obtained from dissociation were then seeded in ultralow attachment dishes in mammary epithelial growth medium again.

Statistical analysis. Results are shown as mean ± s.d. For tumour incidence, the *P* value was calculated using the Fisher's exact test (Fig. 6a,g,h). Bonferroni correction was applied for multiple comparisons (Fig. 6a,g). For tumour volume, the *P* value was calculated using the Kruskal–Wallis test, followed by *post hoc* Steel–Dwass's multiple comparison test (Fig. 6c). Differences at $P<0.05$ were considered to be significant. Statistical analyses were performed using Excel 2010 with the add-in software.

References

1. Visvader, J. E. & Lindeman, G. J. Cancer stem cells in solid tumours: accumulating evidence and unresolved questions. *Nat. Rev. Cancer* **8,** 755–768 (2008).
2. Bonnet, D. & Dick, J. E. Human acute myeloid leukemia is organized as a hierarchy that originates from a primitive hematopoietic cell. *Nat. Med.* **3,** 730–737 (1997).
3. Al-Hajj, M. *et al.* Prospective identification of tumorigenic breast cancer cells. *Proc. Natl Acad. Sci. USA* **100,** 3983–3988 (2003).
4. Ginestier, C. *et al.* ALDH1 is a marker of normal and malignant human mammary stem cells and a predictor of poor clinical outcome. *Cell Stem Cell* **1,** 555–567 (2007).
5. Jiang, F. *et al.* Aldehyde dehydrogenase 1 is a tumour stem cell-associated marker in lung cancer. *Mol. Cancer Res.* **7,** 330–338 (2009).
6. van den Hogen, C. *et al.* High aldehyde dehydrogenase activity identifies tumour-initiating and metastasis-initiating cells in human prostate cancer. *Cancer Res.* **70,** 5163–5173 (2010).
7. Hinohara, K. *et al.* ErbB receptor tyrosine kinase/NF-κB signaling controls mammosphere formation in human breast cancer. *Proc. Natl Acad. Sci. USA* **109,** 6584–6589 (2012).
8. Dontu, G. *et al. In vitro* propagation and transcriptional profiling of human mammary stem/progenitor cells. *Genes Dev.* **17,** 1253–1270 (2003).
9. Takebe, N. & Ivy, S. P. Controversies in cancer stem cells: targeting embryonic signaling pathways. *Clin. Cancer Res.* **16,** 3106–3112 (2010).
10. Scheel, C. *et al.* Paracrine and autocrine signals induce and maintain mesenchymal and stem cell states in the breast. *Cell* **145,** 926–940 (2011).
11. Takabe, K., Paugh, S. W., Milstian, S. & Spiegel, S. 'Inside-out' signalling of sphingosine-1-phosphate: therapeutic targets. *Pharmacol. Rev.* **60,** 181–195 (2008).
12. Kohama, T. *et al.* Molecular cloning and functional characterization of murine sphingosine kinase. *J. Biol. Chem.* **273,** 23722–23728 (1998).
13. Liu, H. *et al.* Molecular cloning and functional characterization of a novel mammalian sphingosine kinase type 2 isoform. *J. Biol. Chem.* **275,** 19513–19520 (2000).
14. Pyne, N. J. & Pyne, S. Sphingosine 1 phosphate and cancer. *Nat. Rev. Cancer* **10,** 489–503 (2010).
15. Fyrst, H. & Saba, J. D. An update on sphingosine-1-phosphate and other sphingolipid mediators. *Nat. Chem. Biol.* **6,** 489–497 (2010).
16. Nagahashi, M. *et al.* Sphingosine-1-phosphate produced by sphingosine kinase 1 promotes breast cancer progression by stimulating angiogenesis and lymphangiogenesis. *Cancer Res.* **72,** 726–735 (2012).
17. Charafe-Jauffret, E. *et al.* Breast cancer cell lines contain functional cancer stem cells with metastatic capacity and a distinct molecular signature. *Cancer Res.* **69,** 1302–1313 (2009).
18. Hirata, N., Sekino, Y. & Kanda, Y. Nicotine increases cancer stem cell population in MCF-7 cells. *Biochem. Biophys. Res. Commun.* **403,** 138–143 (2010).
19. Long, J. S. *et al.* Sphingosine 1-phosphate receptor 4 uses HER2 (ERBB2) to regulate extracellular signal regulated kinase-1/2 in MDA-MB-453 breast cancer cells. *J. Biol. Chem.* **285,** 35957–35966 (2010).
20. Lin, C. I., Chen, C. N., Lin, P. W. & Lee, H. Sphingosine-1-phosphate regulates inflammation-related genes in human endothelial cells thorough S1P1 and S1P3. *Biochem. Biophys. Res. Commun.* **355,** 895–901 (2007).
21. Murakami, A. *et al.* Sphingosine 1-phosphate (S1P) regulates vascular contraction via S1P3 receptor: investigation based on a new S1P3 receptor antagonist. *Mol. Pharmacol.* **77,** 704–713 (2010).
22. Pannuti, A. *et al.* Targeting Notch to target cancer stem cells. *Clin. Cancer Res.* **16,** 3141–3152 (2010).
23. Noseda, M. *et al.* Smooth muscle α-actin is a direct target of Notch/CSL. *Circ. Res.* **98,** 1468–1470 (2006).
24. Jefflies, S., Robins, D. J. & Capobianco, A. J. Characterization of a high-molecular-weight Notch complex in the nucleus of $Notch^{ic}$-transformed RKE cells and in a human T-cell leukemia cell line. *Mol. Cell. Biol.* **22,** 3927–3941 (2002).
25. Artavanis-Tsakonas, S. & Muskavitch, M. A. Notch: the past, the present, and the future. *Curr. Top. Dev. Biol.* **92,** 1–29 (2010).
26. Ladi, E. *et al.* The divergent DSL ligand Dll3 does not activate Notch signaling but cell autonomously attenuates signaling induced by other DSL ligands. *J. Cell Biol.* **170,** 983–992 (2005).
27. Liu, C. *et al.* TACE-mediated ectodomain shedding of the type I TGF-β receptor downregulates TGF-β signaling. *Mol. Cell* **35,** 25–36 (2009).
28. Lammich, S. *et al.* Constitutive and regulated α-secretase cleavage of Alzheimer's amyloid precursor protein by a disintegrin metalloprotease. *Proc. Natl Acad. Sci. USA* **96,** 3922–3927 (1999).
29. Diaz-Rodriguez, E. *et al.* Extracellular signal-regulated kinase phosphorylates tumour necrosis factor alpha-converting enzyme at threonine 735: a potential role in regulated shedding. *Mol. Biol. Cell* **13,** 2031–2044 (2002).
30. Fan, H., Turck, C. W. & Derynck, R. Characterization of growth factor-induced serine phosphorylation of tumour necrosis factor-alpha converting enzyme and of an alternatively translated polypeptide. *J. Biol. Chem.* **278,** 18617–18627 (2003).
31. Xu, P. & Derynck, R. Direct activation of TACE-mediated ectodomain shedding by p38 MAP kinase regulates EGF receptor-dependent cell proliferation. *Mol. Cell* **37,** 551–566 (2010).
32. Pitson, S. M. *et al.* Phosphorylation-dependent translocation of sphingosine kinase to the plasma membrane drives its oncogenic signaling. *J. Exp. Med.* **201,** 49–54 (2005).
33. Igarashi, N. *et al.* Sphingosine kinase 2 is a nuclear protein and inhibits DNA synthesis. *J. Biol. Chem.* **278,** 46832–46839 (2003).
34. Takabe, K. *et al.* Estradiol induces export of sphingosine 1-phosphate from breast cancer cells via ABCC1 and ABCG2. *J. Biol. Chem.* **285,** 10477–10486 (2010).
35. Kawahara, A. *et al.* The sphingolipid transporter spns2 functions in migration of zebrafish myocardial precursors. *Science* **323,** 524–527 (2009).
36. Pébay, A. *et al.* Essential roles of sphingosine-1-phosphate and platelet-derived growth factor in the maintenance of human embryonic stem cells. *Stem Cells* **23,** 1541–1548 (2005).
37. Pitson, S. M. & Pébay, A. Regulation of stem cell pluripotency and neural differentiation by lysophospholipids. *Neurosignals* **17,** 242–254 (2009).
38. Bozkulak, E. C. & Weinmaster, G. Selective use of ADAM10 and ADAM17 in activation of Notch1 signaling. *Mol. Cell. Biol.* **29,** 5679–5695 (2009).
39. van Tetering, G. *et al.* Metalloprotease ADAM10 is required for Notch1 site 2 cleavage. *J. Biol. Chem.* **284,** 31018–31027 (2009).
40. Lu, J. *et al.* Endothelial cells promote the colorectal cancer stem cell phenotype through a soluble form of Jagged-1. *Cancer Cell* **23,** 171–185 (2013).
41. Inoue, A. *et al.* TGFα shedding assay: an accurate and versatile method for detecting GPCR activation. *Nat. Methods* **9,** 1021–1029 (2012).
42. Harrison, H. *et al.* Regulation of breast cancer stem cell activity by signaling through the Notch 4 receptor. *Cancer Res.* **70,** 709–718 (2010).
43. Ruckhäberle, E. *et al.* Microarray analysis of altered sphingolipid metabolism reveals prognostic significance of sphingosine kinase 1 in breast cancer. *Breast Cancer Res. Treat.* **112,** 41–52 (2008).
44. Watson, C. *et al.* High expression of sphingosine 1-phosphate receptors, S1P1 and S1P3, sphingosine kinase 1, and extracellular signal-regulated kinase-1/2 is associated with development of tamoxifen resistance in estrogen receptor-positive breast cancer patients. *Am. J. Pathol.* **177,** 2205–2215 (2010).
45. Long, J. S. *et al.* Sphingosine kinase 1 induces tolerance to human epidermal growth factor receptor 2 and prevents formation of a migratory phenotype in response to sphingosine 1-phosphate in estrogen receptor-positive breast cancer cells. *Mol. Cell. Biol.* **30,** 3827–3841 (2010).
46. Goetzl, E. J. *et al.* Dual mechanisms for lysophospholipid induction of proliferation of human breast carcinoma cells. *Cancer Res.* **59,** 4732–4737 (1999).
47. Ranganathan, P., Weaver, K. L. & Capobianco, A. J. Notch signaling in solid tumours: a little bit of everything but not all the time. *Nat. Rev. Cancer* **11,** 338–351 (2011).
48. Debeb, B. G. *et al.* Pre-clinical studies of Notch signaling inhibitor RO4929097 in inflammatory breast cancer cells. *Breast Cancer Res. Treat.* **134,** 495–510 (2012).
49. Ramakrishnan, V. *et al.* MRK003, a γ-secretase inhibitor exhibits promising *in vitro* pre-clinical activity in multiple myeloma and non-Hodgkin's lymphoma. *Leukemia* **26,** 340–348 (2012).
50. Olsauskas-Kuprys, R., Zlobin, A. & Osipo, C. Gamma secretase inhibitors of Notch signaling. *OncoTargets Ther.* **6,** 943–955 (2013).
51. Kanda, Y., Mizuno, K., Kuroki, Y. & Watanabe, Y. Thrombin-induced p38 mitogen-activated protein kinase activation is mediated by epidermal growth factor receptor transactivation pathway. *Br. J. Pharmacol.* **132,** 1657–1664 (2001).
52. Rao, S., Liu, X., Freedman, B. D. & Behrens, E. M. Spleen tyrosine kinase (Syk)-dependent calcium signals mediate efficient CpG-induced exocytosis of tumour necrosis factor α (TNFα) in innate immune cells. *J. Biol. Chem.* **288,** 12448–12458 (2013).
53. Farmery, M. R. *et al.* Partial purification and characterization of gamma-secretase from post-mortem human brain. *J. Biol. Chem.* **278,** 24277–24284 (2003).

54. Don, A. S. *et al.* Essential requirement for sphingosine kinase 2 in a sphongolipid apoptosis pathway activated by FTY720 analogues. *J. Biol. Chem.* **282,** 15833–15842 (2007).
55. Zhou, J. *et al.* Activation of the PTEN/mTOR/STAT3 pathway in breast cancer stem-like cells is required for viability and maintenance. *Proc. Natl Acad. Sci. USA* **104,** 16158–16163 (2007).
56. Ahn, G. & Brown, J. M. Matrix metalloproteinase-9 is required for tumour vasculogenesis but not for angiogenesis: role of bone marrow-derived myelomonocytic cells. *Cancer Cell* **13,** 193–205 (2008).
57. Prasmickaite, L. *et al.* Aldehyde dehydrogenase (ALDH) activity does not select for cells with enhanced aggressive properties in malignant melanoma. *PLoS ONE* **5,** e10731 (2010).

Acknowledgements

We thank Dr Taro Okada for his helpful comments on the manuscript. We thank Stuart M. Pitson (University of Adelaide), Taro Okada (Kobe University), Aly Karsan (British Columbia Cancer Research Centre), Anthony J. Capobianco (University of Pennsylvania), Spyros Artavanis-Tsakonas (Harvard Medical School), Stefan Lichtenthaler (Ludvig Maximilians University), Lothar J. Strobl (German Research Center for Environmental Health), Michael J. Hendzel (University of Alberta), Rik Derynck (University of California, San Francisco), and J. Silvio Gutkind (National Institutes of Health) for providing the plasmids. We thank Dr Junya Kanda (Jichi Medical University) for assistance with statistical analyses. We also thank additional members of the laboratory and other members of the Institute for their advice and discussion. This work was supported by the Advanced research for medical products Mining Programme of the National Institute of Biomedical Innovation (NIBIO, #09-02 to Y.K.), a Grant-in-Aid for Scientific Research from the Ministry of Education, Culture, Sports, Science, and Technology, Japan (#23590322, #26670041 to Y.K.), a Health and Labour Sciences Research Grant from the Ministry of Health, Labour and Welfare, Japan (Y.K.), and a grant from the Smoking Research Foundation (Y.K.).

Author contributions

N.H. performed most of the experiments. Y.K. planned the project. Y.K. and Y.S. wrote the manuscript. S.Y. performed the experiments related to ADAM17 mutants. T.S. and M.K. performed the experiments related to TY52156. All authors participated in the preparation of the manuscript.

Additional information

Accession codes: Microarray data have been deposited in the NCBI Gene Expression Omnibus database under accession codes GSE59653.

Supplementary Information accompanies this paper at http://www.nature.com/naturecommunications

Competing financial interests: The authors declare no competing financial interests.

Reprints and permission information is available online at http://npg.nature.com/reprintsandpermissions/

How to cite this article: Hirata, N. *et al.* Sphingosine-1 phosphate promotes expansion of cancer stem cells via S1PR3 by a ligand-independent Notch activation. *Nat. Commun.* 5:4806 doi: 10.1038/ncomms5806 (2014).

Journal of Molecular and Cellular Cardiology 77 (2014) 178–191

Contents lists available at ScienceDirect

Journal of Molecular and Cellular Cardiology

journal homepage: www.elsevier.com/locate/yjmcc

Original article

Image-based evaluation of contraction–relaxation kinetics of human-induced pluripotent stem cell-derived cardiomyocytes: Correlation and complementarity with extracellular electrophysiology

Tomohiro Hayakawa [a,*,1], Takeshi Kunihiro [a,1], Tomoko Ando [b], Seiji Kobayashi [a], Eriko Matsui [a], Hiroaki Yada [a], Yasunari Kanda [b], Junko Kurokawa [b], Tetsushi Furukawa [b,**]

[a] Medical Business Unit, Sony Corporation, 1-5-45 Yushima, Bunkyo-ku, Tokyo 113-8510, Japan
[b] Department of Bio-informational Pharmacology, Medical Research Institute, Tokyo Medical and Dental University, 1-5-45 Yushima, Bunkyo-ku, Tokyo 113-8510, Japan

ARTICLE INFO

Article history:
Received 27 July 2014
Accepted 10 September 2014
Available online 23 September 2014

Keywords:
Human-induced pluripotent stem cell-derived cardiomyocytes
Motion vector prediction
Traction force microscopy
Ca^{2+} transient
Field potential
Multi-electrode arrays

ABSTRACT

In this study, we used high-speed video microscopy with motion vector analysis to investigate the contractile characteristics of hiPS-CM monolayer, in addition to further characterizing the motion with extracellular field potential (FP), traction force and the Ca^{2+} transient. Results of our traction force microscopy demonstrated that the force development of hiPS-CMs correlated well with the cellular deformation detected by the video microscopy with motion vector analysis. In the presence of verapamil and isoproterenol, contractile motion of hiPS-CMs showed alteration in accordance with the changes in fluorescence peak of the Ca^{2+} transient, i.e., upstroke, decay, amplitude and full-width at half-maximum. Simultaneously recorded hiPS-CM motion and FP showed that there was a linear correlation between changes in the motion and field potential duration in response to verapamil (30–150 nM), isoproterenol (0.1–10 μM) and E-4031 (10–50 nM). In addition, tetrodotoxin (3–30 μM)-induced delay of sodium current was corresponded with the delay of the contraction onset of hiPS-CMs. These results indicate that the electrophysiological and functional behaviors of hiPS-CMs are quantitatively reflected in the contractile motion detected by this image-based technique. In the presence of 100 nM E-4031, the occurrence of early after-depolarization-like negative deflection in FP was also detected in the hiPS-CM motion as a characteristic two-step relaxation pattern. These findings offer insights into the interpretation of the motion kinetics of the hiPS-CMs, and are relevant for understanding electrical and mechanical relationship in hiPS-CMs.

1. Introduction

Human-induced pluripotent stem cell-derived cardiomyocytes (hiPS-CMs) and human embryonic stem cell-derived cardiomyocyte (hES-CMs) hold promise for the applications in cardiac cell biology [1], drug development [2–6] and cardiac therapeutics [7–11]. To date, hiPS-/hES-CMs have been characterized largely based on studies that examined the aspects of the electrophysiology or the Ca^{2+} signaling/handling [3,12–20]. This is in contrast to the contractile characteristics of the hiPS-/hES-CMs, as there have been few studies performed at the present time [21–29]. Limited numbers of studies, however, demonstrated that hES-CMs showed chronotropy but no significant inotropy in response to β-adrenoceptor agonist, isoproterenol, by using a force transducer for three-dimensionally (3D) engineered hES-CM tissue [29] or for co-culture system of hES-CMs with non-contractile slices of neonatal murine ventricles [28]. These results suggest the importance of performing a phenotype evaluation for hiPS-/hES-CMs based on the contractile properties as well as electrophysiological characteristics to assess their adaptability to the applications. In addition, a report that used atomic force microscopy to investigate two-dimensionally (2D) cultured hiPS-CMs from patients with dilated cardiomyopathy (DCM) demonstrated that the DCM hiPS-CM exhibited a phenotype that was based on the perturbed contractility rather than on the electrophysiological abnormality [27,30]. This demonstrated the need for developing methodologies that characterize the electrical and mechanical relationship of hiPS-/hES-CMs.

In our current study, we combined phase-contrast video microscopy and multi-electrode array (MEA) measurement in order to investigate the relationship between the contractile motion and the extracellular

Abbreviations: ADD, average deformation distance; CM, cardiomyocyte; CRD, contraction–relaxation duration; FP, field potential; FPD, field potential duration; FP_{slow}, slow signal component of FP; FWHM, full-width at half-maximum; hiPS-CM, human-induced pluripotent stem cell-derived cardiomyocyte; hES-CM, human embryonic stem cell-derived cardiomyocyte; MCS, maximum contraction speed; MEA, multi-electrode array; MRS, maximum relaxation speed; PIV, particle image velocimetry; TF, traction force; TFM, traction force microscopy; TTX, tetrodotoxin.

* Corresponding author. Tel.: +81 3 5803 4791; fax: +81 3 5803 4790.
** Corresponding author. Tel.: +81 3 5803 4950; fax: +81 3 5803 0364.
E-mail addresses: tomohiro.hayakawa@jp.sony.com (T. Hayakawa), t_furukawa.bip@mri.tmd.ac.jp (T. Furukawa).
[1] These authors contributed equally.

http://dx.doi.org/10.1016/j.yjmcc.2014.09.010

electrophysiology of the 2D-cultured hiPS-CMs under various cardioactive agents. The label-free video microscopy is a method of choice for evaluating the contractile characteristics of CMs, and many researchers have reported the applicability in various culture conditions [31–40]. For example, for isolated rod-shaped adult CMs, the shortening length and velocity of contraction of whole cell body or sarcomere were evaluated quantitatively using video microscopy with edge-detection technique [34,41–43]. Edge-detection method was also applied to the contractility estimation of embryonic bodies with hES-CMs [44,45]. Kamgoue et al. applied image correlation analysis for single adult and neonatal rat CMs, and detected intracellular strains quantitatively from the calculated 2D displacement field [36]. Modified image correlation analysis was developed by Ahola et al. for single hiPS-CMs, which exhibits heterogeneous in shape, to evaluate the detailed intracellular deformation [46]. Beating frequency of mouse ES-CM monolayer has been evaluated based on the image analysis of transmitted light intensity change [35] and the fast Fourier transform technique [39]. Meanwhile, we have previously reported the applicability of image correlation analysis, or motion vector analysis, for analyzing video images of neonatal rat CM monolayers [47]. By calculating the velocity field over the whole image, this method has made it possible to evaluate the average contractile speed, global deformation and contraction propagation in the CM monolayer with high spatiotemporal resolution [47]. Due to the convenience and non-invasiveness, such label-free video microscopies would be advantageous for the readout method of hiPS-/hES-CM behaviors, especially for the applications in therapeutics and drug safety assessment. In addition, since microscope observation itself does not interfere with the electrophysiological measurements, video microscopies are amenable to the simultaneous measurement with electrical measurements, e.g., patch clamping and MEA, to gain greater insight into the electro-mechanical correlations of CMs.

In this study, we further performed traction force microscopy and Ca^{2+} imaging in the hiPS-CMs in order to discuss the association of contractile motion to force development and Ca^{2+} transient, respectively. Our results showed that electrophysiological and functional behaviors of the 2D-cultured hiPS-CMs are quantitatively reflected by contractile motions detected with high-speed video microscopy. These findings offer insights into the interpretation of motion kinetics of hiPS-CMs, and are relevant for understanding electrical and mechanical relationship in hiPS-CMs. These results also demonstrate that it is possible for us to broaden the scope of application for hiPS-CMs for use in even simple culture conditions.

2. Materials and methods

2.1. hiPS-CMs and cell preparation

The hiPS-CMs used in this study were purchased from Cellular Dynamics International, Inc. (CDI) (iCell Cardiomyocytes, CDI, Madison, WI, USA). The iCell CMs are highly purified human CMs (>98% pure cardiomyocytes) that are derived from iPS cells using previously described differentiation and purification protocols [48]. The iCell CMs were seeded and maintained according to the protocol recommended by the supplier using iCell Cardiomyocytes Plating Medium (CDI) and iCell Cardiomyocytes Maintenance Medium (CDI) at 37 °C, 7% CO_2. The details on the cell preparation for MEA recordings, Ca^{2+} transient measurements and TFM are provided in the Supplementary materials.

2.2. Video microscopy

A high-speed digital CMOS camera (KP-FM400WCL, Hitachi Kokusai Denki Engineering, Tokyo, Japan) was mounted on an inverted microscope (Eclipse Ti, Nikon, Tokyo, Japan). Movie images of beating hiPS-CMs were recorded as sequential phase-contrast images with a 10× objective at a frame rate of 150 fps, a resolution of 2048 × 2048 pixels, and a depth of 8 bits. Further details on the video imaging are provided in the Supplementary materials.

2.3. Motion vector analysis

Motion vectors of beating hiPS-CMs were obtained using a block matching algorithm, as has been described elsewhere [47,49]. Further details on the motion vector analysis are provided in the Supplementary materials.

2.4. Traction force microscopy

2.4.1. Fabrication of polyacrylamide hydrogel substrates and hiPS-CM seeding

Polyacrylamide hydrogel substrates containing fluorescence beads (#G0100, 1 μm diameter, Ex/Em = 468/508 nm, Duke Scientific Co., CA, USA) were fabricated in accordance with previously reported methods [26,50,51]. Further details on the methods are provided in the Supplementary materials.

2.4.2. Traction force microscopy

Video of the hiPS-CMs cultured on polyacrylamide gel was captured using phase-contrast and fluorescence microscopy to detect contractile motion and substrate deformation, respectively. Estimation of the force development of hiPS-CMs was performed by a particle image velocimetry (PIV) [52] and Fourier transform traction cytometry (FTTC) [51–53] programs implemented as an ImageJ plugin. Details are provided in the Supplementary materials.

2.5. Simultaneous recordings of FP and motion

MED probes (MED-P515A, Alpha MED Sciences, Osaka, Japan) equipped with platinum black-coated 64 planar microelectrodes that were arranged in an 8 × 8 grid embedded in the center of a transparent glass plate were used for extracellular recordings of the FP from the CM monolayer [54]. The details on the cell preparation for MEA recordings are provided in the Supplementary materials. Image acquisitions and multi-electrode array (MEA) recordings were synchronized using external triggering options of the MEA system. Data were recorded simultaneously for the 64 electrodes (sampling frequency; 20 kHz, bandwidth; 1–1000 Hz) and were analyzed by Mobius Software (Alpha MED Sciences) in order to detect the field potential duration (FPD). In this study, we averaged at least 10 consecutive FP waveforms to evaluate the field potential parameters. The details on the simultaneous measurements are also provided in the Supplementary materials.

2.6. Calcium imaging

For imaging of the Ca^{2+} transient in the hiPS-CMs, iCell Cardiomyocytes (CDI) were plated in a 96-well plate pre-coated with rat collagen type I (BD, Franklin lakes, NJ) at a density of 3×10^4 cells/well (cultured with 100 μl medium). hiPS-CMs were loaded with Fluo-5F/AM (Invitrogen, Carlsbad, CA, USA) dissolved in dimethylsulfoxide (DMSO, WAKO Pure Chemical, Osaka, Japan) and added to the culture medium at a concentration of 5 μM in preparation for the Ca^{2+} imaging. After 30 min incubation, the culture dishes were placed on a microscope stage (IX-71, Olympus, Tokyo, Japan). Ca^{2+} fluorescence images were captured with a digital CCD camera (CoolSNAP HQ2, Photometrics, Tucson, AZ, USA) at a resolution of 696 × 520 pixels and 33 fps using a 20× objective and recorded using MetaMorph software (Molecular Devices, Sunnyvale, CA, USA). The data were then quantified as the background subtracted fluorescence intensity changes (ΔF) normalized to the baseline fluorescence (F_0) using the ImageJ software and the KaleidaGraph software ver. 4.1.1 (Synergy Software, Reading, PA, USA). Amplitudes, full-width at half-

maximum, maximal upstroke and the decay of the Ca^{2+} transient were also analyzed with the KaleidaGraph software.

2.7. Cardioactive substances

Isoproterenol was purchased from Sigma (St. Louis, MO, USA), E-4031 and tetrodotoxin from WAKO Pure Chemical Industries, and verapamil from Nacalai Tesque (Kyoto, Japan). Stock solutions for isoproterenol and E-4031 were prepared in distilled water, while verapamil was prepared in DMSO. All stock solutions were further diluted in culture medium, with the final concentration of DMSO less than 0.05%. Four to six increasing concentrations of the test substances were applied consecutively for 10 min each.

2.8. Statistical analysis

Data are compared to control in the paired *t*-test for the grouped data. Data are presented as means ± SEM. The value was expressed as a percentage of the control value, while the comparison was made using raw values of each parameter. We considered *p* values less than 0.05 to be statistically significant.

3. Results

3.1. Motion vector detection as a reliable representation of contractile characteristics of hiPS-CMs

3.1.1. Motion vector detection from the movie image of single hiPS-CMs

We first evaluated the contractile motion of single hiPS-CMs. Sparsely plated hiPS-CMs exhibited heterogeneous shapes and a variety of sizes (Fig. 1A). Fig. 1B shows an example of single hiPS-CM motion detected by the motion vector analysis. As indicated by the motion vectors that overlay the image of hiPS-CM, cellular deformation generally occurred toward the center direction of the cell body during contraction process (Fig. 1B (1)). After a transient pause of cellular motion (Fig. 1B (2)), the cell body returned to the position of resting state, exhibiting a slower motion speed than that observed during contraction (Fig. 1A (3)). By averaging the magnitude of motion vectors and plotting them against time, we were able to obtain information on the contraction and relaxation motion (Fig. 1C), along with the frequency (Fig. 1D). Although the contraction and relaxation occurs in the opposite direction, the average of vector magnitude is a positive value, thereby resulting in a two-positive peak profile that reflects the contraction–relaxation process. As seen in Fig. 1E, we are able to extract various parameters regarding contractile motion from this two-peak motion profile. Our current study primarily examined four parameters of this hiPS-CM motion. These included the maximum values of the average magnitude of motion vectors during the contraction (a) and relaxation (b) processes (termed MCS; maximum contraction speed and MRS; maximum relaxation speed, respectively), the total area under two peaks (c) (representing the average deformation distance (ADD) during the contraction–relaxation process), and the duration of contraction and relaxation motion (d) (with the duration between the onset of the contraction peak and the offset of the relaxation peak defined as the contraction–relaxation duration (CRD)). Fig. 1F–I shows contractile parameters of single hiPS-CMs ($n = 40$) cultured in physiological condition (37 °C and 5% CO_2). Single hiPS-CMs exhibited beating rate ranging from ~20 to ~110 beats per minute (bpm) with the average of 62 bpm. Analysis of motion vectors showed that the average values of MCS, MRS, CRD and ADD were 8.2 μm/s, 4.1 μm/s, 455 ms and 1.07 μm, respectively, and the average cell area was found to be 4244.3 μm^2. We examined to plot the cell area against MCS and MRS, and found that contractile speeds were not significantly dependent on the cell area (Fig. 1K). CRD of single hiPS-CMs showed a linear correlation with the beating rate with the correlation coefficient of 0.768 (Fig. 1L).

3.1.2. Contractile motion and traction force of the hiPS-CMs

Subsequently, we used traction force microscopy (TFM) to assess whether the cellular deformation, detected by phase-contrast microscopy and motion vector analysis, was correlated with the force development of hiPS-CMs on the elastic substrate (polyacrylamide gel). Fig. 2 shows a typical image of a hiPS-CM on the gel substrate (12 kPa) examined by phase-contrast (a) and fluorescence microscopy (b). Typical images of displacement and traction force fields that were calculated from the two fluorescence images (taken before and after contraction) are also shown in Fig. 2A(c) and (d), respectively. We then compared the ADD and the traction force of hiPS-CMs on the elastic substrate (12 kPa and 50 kPa). As shown in Fig. 2B, a linear correlation was observed for the traction force and the ADD of the single hiPS-CMs cultured on gel substrates, with a correlation coefficient of 0.737 ($n = 13$) and 0.595 ($n = 12$) for the hiPS-CMs on the 12 kPa and 50 kPa substrates, respectively. These results suggested that the cellular deformation detected with motion vector analysis could be used as a surrogate of the traction force developed by the hiPS-CM contraction.

3.1.3. Ca^{2+} transient and contractile motion of hiPS-CMs

To verify the relationship between the contractile motion and the cytoplasmic Ca^{2+} concentration, we further examined the parameters of the Ca^{2+} transient of the hiPS-CMs. Fig. 3A and B show the typical examples of Ca^{2+} transient and motion waveform of hiPS-CMs, respectively, in the absence and the presence of 100 nM isoproterenol. Isoproterenol altered the amplitude, maximum upstroke, maximum decay and full-width at half-maximum (FWHM) of the Ca^{2+} transient with 113, 114, 157 and 84% of the control, respectively (see bar charts in Fig. 3A). Isoproterenol also altered the contractile parameters, i.e., ADD, MCS, MRS and CRD were changed to 113, 124, 146 and 80% of the control, respectively (Fig. 3B). In contrast, verapamil (100 nM) decreased all of the parameters of Ca^{2+} transient and contractile motion except the decay of Ca^{2+} transient (Fig. 3C and D). As shown in the bar charts in Fig. 3C and D, verapamil altered the Ca^{2+} transient amplitude, upstroke, decay and FWHM with 63, 78, 97 and 66%, respectively, while ADD, MCS, MRS and CRD with 52, 62, 63 and 66%, respectively. These results suggested that the contractile parameters of hiPS-CMs correspond to the intracellular Ca^{2+} status.

3.2. Correlation between the FP and the contractile motion of hiPS-CMs

We next performed a simultaneous recording of the contractile motion and FP using a hiPS-CM monolayer cultured in a MEA dish. To accurately evaluate the relationship between the motion and the FP of hiPS-CMs, the motion vectors were calculated from the hiPS-CMs that were located close to the vicinity of the electrode used for FP data collection. The yellow-squared area (150 × 150 μm) in Fig. 4A represents an example of the region that was used for evaluating contractile motion. Fig. 4B is an enlarged image, in which the calculated motion vectors (fine white bars) are overlaid on the image of the yellow-squared region shown in Fig. 4A. The MCS was ~10 to ~20 μm/s in normal culture conditions (e.g., 37 °C, 5% CO_2 and ~100% humidity) in the absence of any drugs. The simultaneously measured FP exhibited a typical waveform that had a sharp initial negative deflection, which is supposedly correlated with the inward Na^+ current. This is followed by a broad negative deflection (FP_{slow}) and a terminal positive deflection, which is supposedly correlated with the inward Ca^{2+} and outward K^+ currents, respectively [55–58]. As seen in the waveforms presented in Fig. 4C, D and E, several features of the relationship between the motion and the FP of hiPS-CMs were identifiable. These included 1) the CRD was longer than the FPD. The end of the FPD was previously defined as either the peak of the positive deflection [6,54,55,59] or the point where the positive deflection returns to the baseline [60]. The former end-point appears to be correlated with the upstroke of relaxation motion, while the latter end-point appears to be correlated with the peak of relaxation

motion. However, determination of an accurate end-point of FP proved difficult to establish. Other observed features included 2) the onset of the contraction motion follows the occurrence of the Na^+ current peak of the FP (see Fig. 4E), and 3) the position of FP_{slow} occurs with the contraction. The relationships between the motion profiles and the FP for the hiPS-CM described in 1) and 2) were also found in neonatal rat CMs (Supplementary Fig. 2). However, the point 3) was not observed in rats. In the neonatal rat CMs, the entire FP_{slow} was localized within the contraction motion and the broad positive deflection of the FP positions near the end of contraction motion (Supplementary Fig. 2B).

3.3. Correlation between the FP and the contractile motion of hiPS-CMs in the presence of drugs

To determine the correspondence between the contractile motion of the hiPS-CMs and the electrophysiological behavior obtained by the MEA technique, we examined various drugs that are known to inhibit Na^+, K^+ and Ca^{2+} channels.

3.3.1. The effects of a Na^+ channel blocker, tetrodotoxin (TTX)

It has been reported that Na^+ channel blockers decreased the amplitude and slope of the initial negative spike of FP waveform of CM

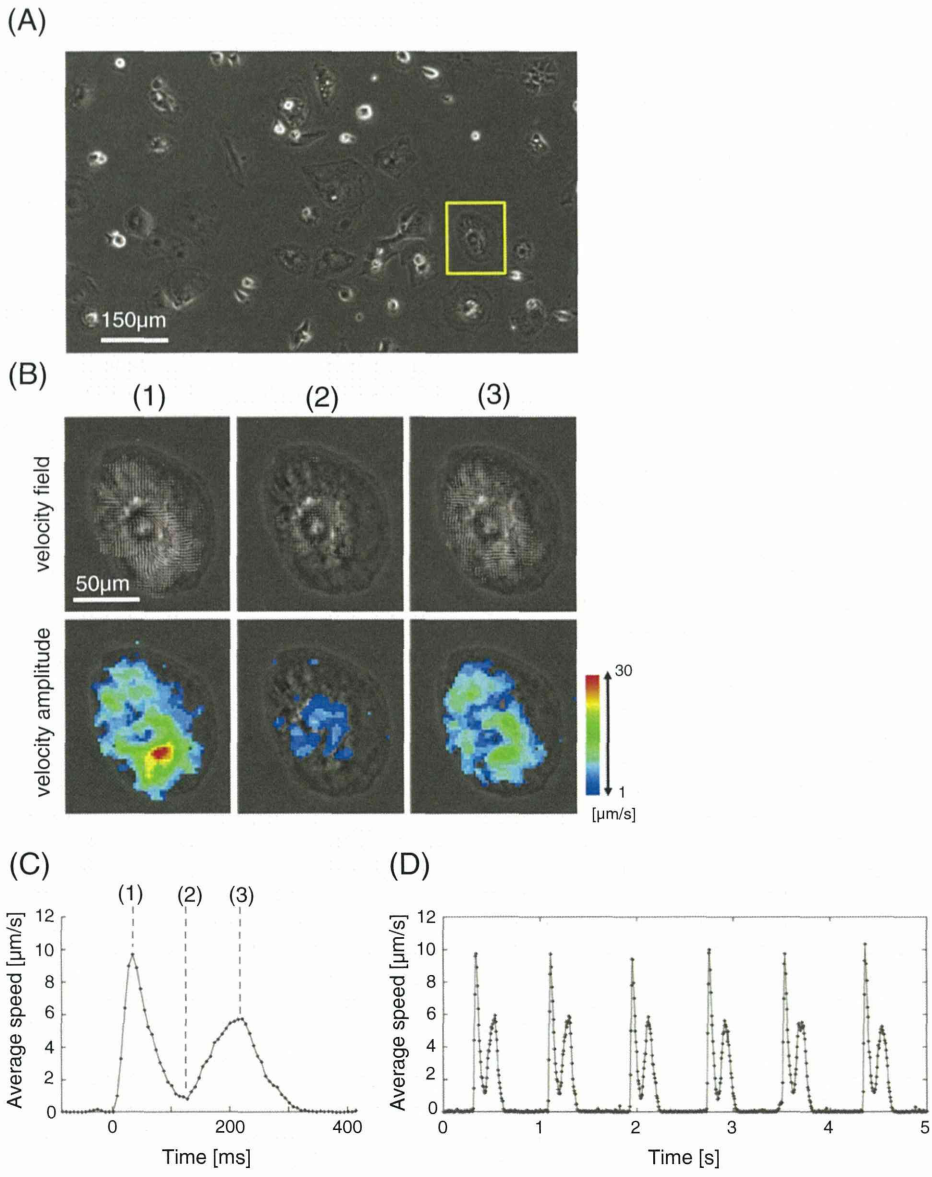

Fig. 1. Motion vectors detected during the contraction and relaxation process of a single hiPS-CM. (A) Example of a phase-contrast image of sparsely plated hiPS-CMs on a collagen-coated polystyrene dish, which was captured using a 10× objective. (B) Contractile motion of the hiPS-CM in the yellow-squared region in (A) was detected using motion vector analysis. In the upper panels, motion vectors show the velocity field at contraction (1), at the end of contraction (2) and at the relaxation (3). Bottom panels show the visualized amplitude of the velocity field in a heat-map style that corresponds to the upper panels. (C) Example of a motion waveform representing contraction and relaxation peaks, calculated with the single hiPS-CM shown in (B). Points (1)–(3) correspond to the same time points in the picture in part (B). (D) The train of motion waveform calculated with the single hiPS-CM shown in (B). (E) Schematics of a motion waveform of CM contraction–relaxation obtained with motion vector analysis. a–c in (E) represent contractile parameters evaluated in the present study, a: maximum contraction speed (MCS), b: maximum relaxation speed (MRS), c: average deformation distance (ADD) and d: contraction–relaxation duration (CRD). (F)–(J) show the summaries of contractile parameters and cell-area of single hiPS-CMs ($n = 40$), evaluated with motion vector analysis. Bars in (F)–(J) represent the average values for each plot. (K) Cell-area dependence of maximum contraction and relaxation speed (MCS and MRS). MCS and MRS were assessed from single hiPS-CMs ($n = 40$) and were plotted against their 2D area. Solid and dotted lines represent linear regression for MCS (black dots) and MRS (gray dots), respectively. (L) Correlation between CRD and the beating rate of single hiPS-CMs ($n = 40$).

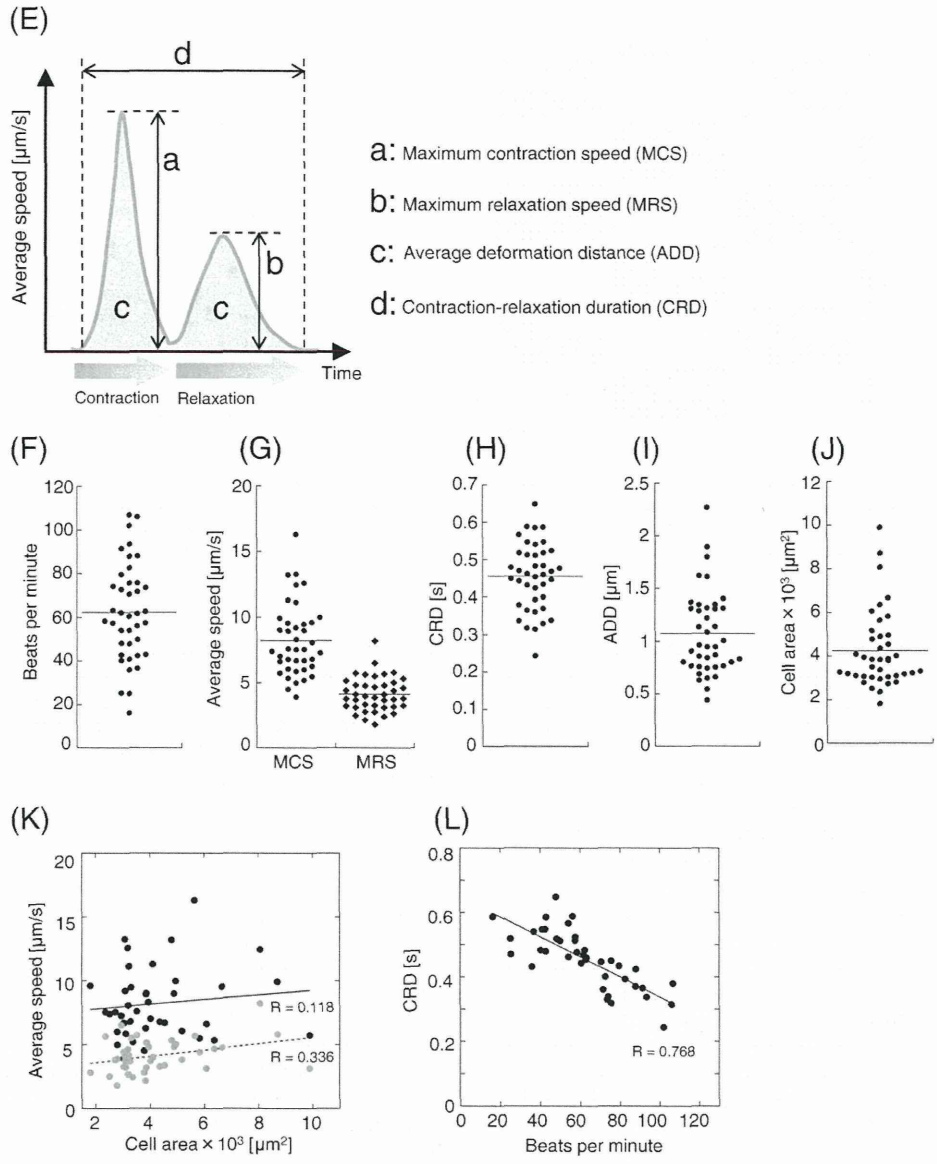

Fig. 1 (*continued*).

cultures [55,58,61]. To confirm the correspondence of these effects on the contractile behaviors of hiPS-CMs, we simultaneously recorded FP and motion of hiPS-CMs in the presence of 0–30 μM of TTX (Fig. 5A). Enlargement of the onset region of Fig. 5A is shown in Fig. 5B. The FP duration from the onset of the positive spike to the peak of the negative spike was significantly prolonged to 161% and 212% of the control at 9 and 30 μM of TTX, respectively, while the FPD measured as the duration between the initial negative peak and the peak of positive deflection increased to 106% and 110% of the control at the same concentrations. Along with the delay of the spikes, the Na^+ peak of FP exhibited broadening and a decrease in the peak slope. The contraction motion also exhibited a delay in the onset and peak position. As shown in Fig. 5C, the durations from the onset of the positive FP spike to the peak of the negative FP spike were linearly correlated with the durations from the onset of the positive FP spike to the onset of the contraction motion peak ($R = 0.856$). Although there was a progressive decrease in the beating rate in accordance with increasing TTX concentrations (Fig. 5G), no major increases in the FPD or CRD were observed (Fig. 5D and G). While the MRS was nearly unaffected, there was a significant decrease in the MCS (Fig. 5E). Despite this major decrease in the MCS, there was no significant alteration in the ADD (Fig. 5F).

3.3.2. The effects of a K^+ channel blocker, E-4031

A K^+ channel (I_{Kr}) blocker, E-4031, prolonged FPD of hiPS-CMs depending on the concentration (Fig. 6A), which is in line with previous reports [54,62]. The motion profile exhibited a prolongation of CRD, with a significant decrease in MRS (Fig. 6A). FPD and CRD showed a linear relationship in the presence of 0–50 nM E-4031 (Fig. 6B) with a correlation coefficient of $R = 0.915$. The slope of the linear regression was 1.362 (FPD/CRD). In the presence of 100 nM E-4031, the hiPS-CMs exhibited an EAD-like FP profile (Fig. 6A and C), i.e., there was an occurrence of negative deflection prior to the positive deflection. Since it was difficult to define the peak point of positive deflection, associated with K^+ current, or FPD in FP waveforms with EAD, we eliminated the data with EAD-like waveform from the evaluation of the CRD–FPD correlation (Fig. 6B). As shown in Fig. 6A and C, the motion profile also exhibited an irregular relaxation pattern that corresponded to the EAD-like FP waveform. This indicates that the speed of the relaxation